Molecular Determinants of Severe Acute Respiratory Syndrome Coronavirus Pathogenesis and Virulence in Young and Aged Mouse Models of Human Disease

Matthew Frieman,[a] Boyd Yount,[b] Sudhakar Agnihothram,[b] Carly Page,[a] Eric Donaldson,[b] Anjeanette Roberts,[c]* Leatrice Vogel,[c] Becky Woodruff,[b]* Diana Scorpio,[d] Kanta Subbarao,[c] and Ralph S. Baric[b]

Department of Microbiology and Immunology, University of Maryland School of Medicine, Baltimore, Maryland, USA[a]; Department of Epidemiology, School of Public Health, University of North Carolina at Chapel Hill, Chapel Hill, North Carolina, USA[b]; Laboratory of Infectious Diseases, NIAID, NIH, Bethesda, Maryland, USA[c]; and Department of Molecular and Comparative Pathology, Johns Hopkins University, Baltimore, Maryland, USA[d]

SARS coronavirus (SARS-CoV) causes severe acute respiratory tract disease characterized by diffuse alveolar damage and hyaline membrane formation. This pathology often progresses to acute respiratory distress (such as acute respiratory distress syndrome [ARDS]) and atypical pneumonia in humans, with characteristic age-related mortality rates approaching 50% or more in immunosenescent populations. The molecular basis for the extreme virulence of SARS-CoV remains elusive. Since young and aged (1-year-old) mice do not develop severe clinical disease following infection with wild-type SARS-CoV, a mouse-adapted strain of SARS-CoV (called MA15) was developed and was shown to cause lethal infection in these animals. To understand the genetic contributions to the increased pathogenesis of MA15 in rodents, we used reverse genetics and evaluated the virulence of panels of derivative viruses encoding various combinations of mouse-adapted mutations. We found that mutations in the viral spike (S) glycoprotein and, to a much less rigorous extent, in the nsp9 nonstructural protein, were primarily associated with the acquisition of virulence in young animals. The mutations in S likely increase recognition of the mouse angiotensin-converting enzyme 2 (ACE2) receptor not only in MA15 but also in two additional, independently isolated mouse-adapted SARS-CoVs. In contrast to the findings for young animals, mutations to revert to the wild-type sequence in nsp9 and the S glycoprotein were not sufficient to significantly attenuate the virus compared to other combinations of mouse-adapted mutations in 12-month-old mice. This panel of SARS-CoVs provides novel reagents that we have used to further our understanding of differential, age-related pathogenic mechanisms in mouse models of human disease.

The severe acute respiratory syndrome coronavirus (SARS-CoV) is a zoonotic pathogen that emerged in Guangdong Province in Southeast China in the fall of 2002 (10). Age was a major cofactor enhancing morbidity, as evidenced by >50% mortality rates in immunosenescent populations >65 years of age, coupled with low mortality rates in individuals <20 years old and medium mortality rates of ~10% for the rest of the population (58). SARS-CoV is a respiratory pathogen, and severe pathology is found in the pulmonary system, with minor lesions/virus titers in the liver, gastrointestinal tract, kidney, skeletal muscle, and lymphoid organs (23, 33, 44). The predominant pathological features of SARS-CoV infection in the human lung are acute lung injury (ALI) leading to diffuse alveolar damage (DAD), hyaline membrane formation, and atypical pneumonia that progresses to acute respiratory distress syndrome (ARDS), with inflammatory exudation in the alveoli and interstitial tissue and with epithelial cell hyperplasia (6, 29, 42, 43, 58). After the acute phase, organizing-phase DAD with increased fibrosis is often observed (44). ALI may progress to ARDS, an inflammatory lung disease with 50% mortality rates that causes ~1,000,000 deaths/year worldwide and ranks among the most difficult challenges in critical care medicine (30). The mechanisms regulating disease progression are unknown, hampering the development of therapies. Thus, a critical need exists for robust animal models of human disease that capture acute end-stage lung disease pathologies, such as DAD and ARDS, following acute virus infection.

SARS-CoV has a ~30-kB single-stranded, positive-polarity RNA genome that is packaged within a helical nucleocapsid composed of multiple copies of the nucleocapsid protein (N) and surrounded by a lipid bilayer that contains several virus glycoproteins, such as the 90/180-kDa spike glycoprotein, the 23-kDa M glycoprotein, and the 12-kDa E protein (49). Two large open reading frames (ORFs) are present at the 5' end of the genome; these are initially expressed as two large polyproteins, which are then processed by two virally encoded proteases, the papain-like protease (PLP) (nonstructural protein 3 [nsp3]) and Mpro (nsp5), into 16 nsp's (nsp1 to nsp16). Among these, nsp3, nsp5, nsp9, and nsp13 have been studied. The nsp3 gene encodes several novel functional or predicted enzymatic activities, including the viral protease PLP, which cleaves nsp1 through nsp3 from the ORF1a polyprotein and has additional interferon antagonist, deubiquitination, and de-ISGylation activities (2, 20, 59). nsp5 encodes the main protease, Mpro, which cleaves nsp4 through nsp16 from the respective precursor polyproteins. nsp9 is an RNA binding pro-
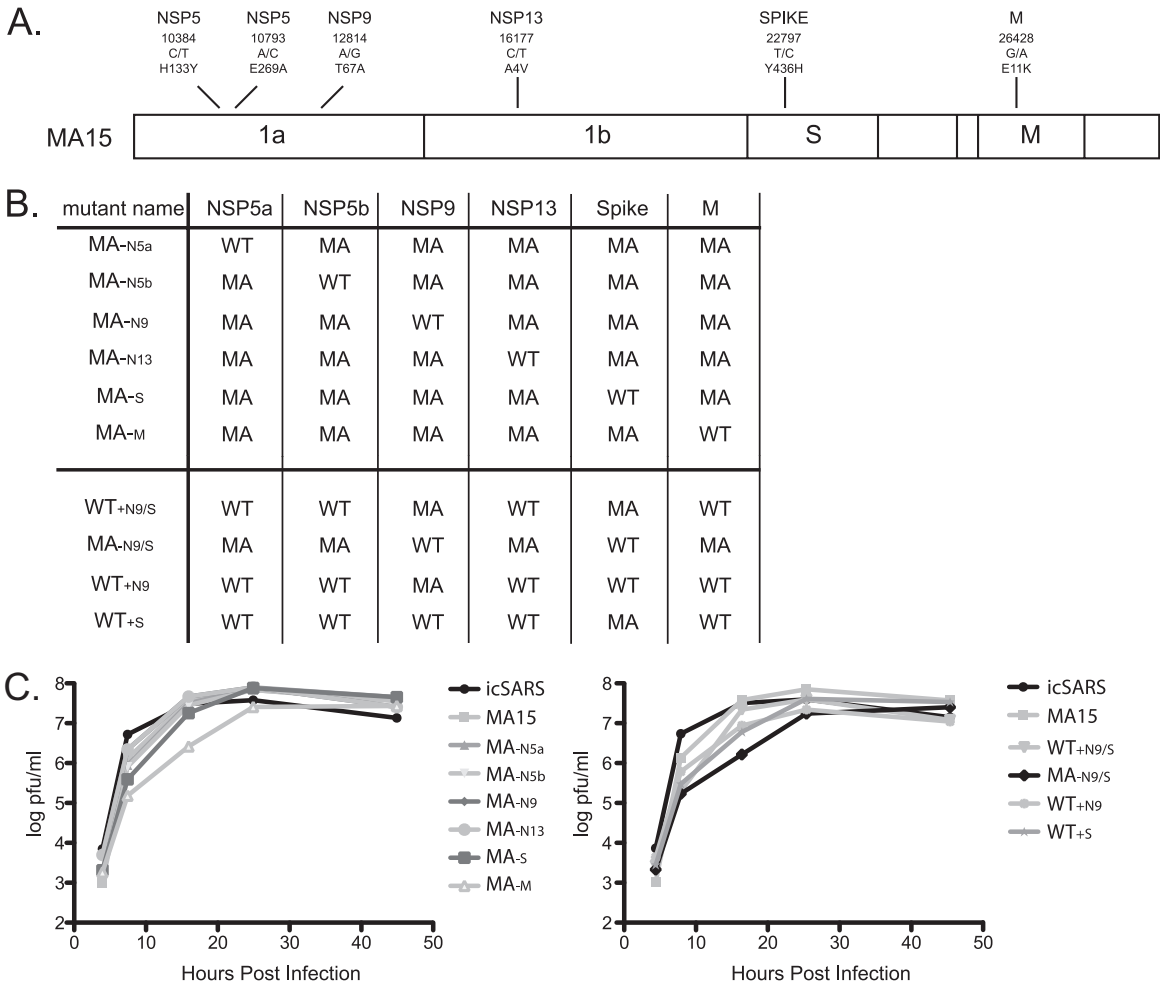
FIG 1 rMA15 viruses. (A) Genomic sequence of rMA15 showing the 6 amino acid changes found in the passaged virus. (B) Chart of rMA15 mutant viruses used in the experiments. In the mutant names, a plus sign means that the virus contains the MA15 amino acid at the position identified, and a minus sign means that the virus contains the WT Urbani amino acid at that position. Under the protein designations, MA indicates an rMA15 mutation at the designated allele, while WT indicates an Urbani amino acid at the designated allele. (C) Growth curves of the mutant viruses in Vero E6 cells, showing efficient replication of the recombinant mutant viruses described in panel B.

tein that is essential for replication, although its exact function still remains unknown (14, 69). nsp13 contains a helicase domain that has also been shown to be important for RNA replication (25, 70). Although these nsp's are clearly essential for efficient virus replication, their direct or indirect contributions to virus cross-species transmission, adaptation, and/or enhanced viral pathogenesis are not clear.

We have developed several robust mouse models for SARS-CoV infection that capture the age-related disease phenotypes seen during acute SARS-CoV infection in humans (53, 55, 56, 63). The epidemic strain of SARS-CoV, the Urbani strain, is minimally pathogenic in young or even aged (12-month-old) mice, as evidenced by limited morbidity and no mortality following infection (18, 55). However, serial passage of the SARS-CoV Urbani strain in 10-week-old BALB/c mice rapidly selected for a mouse-adapted strain of SARS-CoV (called MA15; 15 passages before 100% mortality was produced) that caused death in young and aged BALB/c mice (53). In contrast to the effects of the SARS-CoV parent strain, Urbani, the pulmonary pathology of young mice infected with the MA15 virus showed extensive damage to bronchiolar and alveolar

epithelial cells (53). Viral antigen was highly prevalent in the bronchiolar epithelium, in alveolar pneumocytes, and in necrotic debris deposited within the alveoli and the bronchiolar lumen of mice. In contrast to the findings for transgenic mouse models expressing human angiotensin-converting enzyme 2 (hACE2), no central nervous system (CNS) involvement was observed (53). In aged animals, these changes were more pronounced, as was also true following SARS-CoV Urbani infection, including the development of DAD with visible hyaline membrane formation and inflammation scattered throughout the parenchyma (53, 63).

MA15 contains six mutations in its genome that account for its increased virulence in mice (53, 63). Four of these mutations reside in replicase proteins (2 mutations in nsp5, 1 in nsp9, and 1 in nsp13), and 1 mutation each resides in the S and M glycoprotein structural proteins (Fig. 1A). During the 2003 epidemic, modeling and structural studies indicated that certain mutations in the S protein enhanced interaction with human ACE2 and that a K353H change in mouse ACE2 (mACE2) likely reduced the efficiency of interaction with SARS-CoV, explaining the reduced replication and disease phenotypes in mouse models (36–38, 71). In

this report, our data suggest that the MA15 H436 mutation in the spike glycoprotein afforded efficient interaction with mACE2 to enhance disease outcomes in mouse models of the human disease. Similar adaptation through mutations of S proteins was noted during the emergence of SARS-CoV from zoonotic precursors during the 2002-to-2003 outbreak (19, 67). Using a SARS-CoV molecular clone, we reconstructed a recombinant mouse-adapted SARS-CoV (rMA15) that replicated with growth kinetics identical to those of the original parent virus, MA15, in culture and induced similar clinical disease and pathological changes (53). To evaluate the contributions of different mutations to the pathological outcomes seen in young and aged mice, we constructed a set of derivative recombinant viruses, each containing admixtures of wild-type (WT) and mouse-adapted alleles, designed to identify key residues that contributed to the development of severe clinical disease. Our data demonstrate that the MA15 mouse-adapted mutation in the spike glycoprotein was significantly associated with the development of weight loss and mortality in young animals. nsp9 also had a modest but variable effect on the enhancement of viral pathogenesis. In 12-month-old BALB/c mice, rMA15 caused 100% mortality, and nearly any combination of two or more mouse-adapted alleles tested was associated with increased disease severity and mortality. Using this new model, we identified the molecular changes present in the MA15 virus that lead to its increased pathogenesis in young and aged mouse models of human disease.

MATERIALS AND METHODS

Bioinformatics and structural modeling. The amino acid sequence of the MA15 receptor binding domain (RBD) was aligned to the SARS-CoV Tor2 RBD sequence, for which an X-ray crystal structure has been solved (Protein Data Bank [PDB] accession code 2AJF), using Clustal X, version 1.86. A homology model of MA15 was then generated from this alignment, using the Tor2 RBD sequence as a template in the Modeler program, available as part of the Max Planck Institute Bioinformatics Toolkit (http://toolkit.tuebingen.mpg.de/). The structural models were analyzed and compared using MacPyMOL (Delano Scientific).

Viruses and cells. Vero E6 cells were grown in minimal essential medium (MEM) (Invitrogen, Carlsbad, CA) supplemented with 10% Fetal Clone II (HyClone, South Logan, UT) and gentamicin-kanamycin (UNC Tissue Culture Facility). Stocks of the recombinant mouse-adapted SARS-CoV (rMA15) were propagated; the titers were determined on Vero E6 cells; and the virus was cryopreserved at −80°C until use as described below. All viral and animal experiments were performed in a class II biological safety cabinet in a certified biosafety level 3 laboratory containing redundant exhaust fans, and workers wore personnel protective equipment, including Tyvek suits, hoods, and high-efficiency particle arrestor (HEPA)-filtered powered air-purifying respirators (PAPRs).

Construction of the MA15 derivative recombinant virus panel. A panel of MA15 derivative viruses was created using the previously described infectious clone MA15 (53). The MA15 genome contains six mutations that have been incorporated into the reverse genetic system for SARS-CoV. This system consists of six plasmids that span the entire ~30-kb genome of the virus. To create each of the variant viruses, the SARS-CoV wild-type reverse genetic clone fragment was substituted for a corresponding MA15 fragment, allowing us to create a set of viruses containing various combinations of the MA15 amino acid substitutions.

The production of each virus used the previously described infectious clone system (73). Briefly, each of the six plasmids containing fragments of the SARS-CoV genome were cut with restriction enzymes, and the inserted viral genome piece was gel purified from an agarose gel using QIAquick gel purification (Qiagen). These cDNA fragments were ligated together into a full-length cDNA, and a full-length RNA was generated

from a 5′ T7 polymerase start site using mMessage mMachine as described by the manufacturer (Ambion). Vero E6 cells were electroporated with the different full-length genomic RNAs produced, and the virus was isolated after 1 passage of the supernatant from electroporated cells. The recovered virus was plaque purified and sequenced to confirm that the correct mutations were present in each recombinant virus. All the virus stocks produced displayed consistent phenotypes over repeated *in vivo* infections of mice, indicating that any compensatory mutations elsewhere in the genome were not responsible for the pathogenesis phenotype observed.

***In vivo* infections of young and aged mice.** BALB/c mice were purchased from Charles River at the age of 8 weeks and were used for experiments at the age of 10 weeks. Aged mice were purchased from the National Institute of Aging at the age of 12 months. Mice were anesthetized with a mixture of ketamine-xylazine and were infected intranasally either with the virus or with phosphate-buffered saline (PBS) in a dose of 50 μl. Virus doses ranged from 1×10^2 to 1×10^5 PFU/50-μl dose, diluted in PBS prior to intranasal administration. Animal housing and care were in accordance with all UNC—Chapel Hill Institutional Animal Care and Use Committee (IACUC) guidelines and the University of Maryland at Baltimore Institutional Animal Care and Use Committee guidelines. Infected animals were sacrificed upon approaching 80% of their starting body weight or manifesting severe clinical symptoms, according to the IACUC guidelines.

Histological analysis. Lung tissues were fixed in PBS–4% paraformaldehyde (pH 7.3); tissues were embedded in paraffin; and 5-μm-thick sections were prepared by the UNC histopathology core facility. To determine the extent of inflammation, sections were stained with hematoxylin and eosin (H&E) and were scored in a blinded manner. Sections were scored from 1 to 5 for overall inflammation, eosinophilia, neutrophilia, alveolitis, bronchiolar denudation, and edema.

Statistical analyses. Percentages of starting weights, viral titers, and numbers of inflammatory cells were evaluated for statistically significant differences by the nonparametric Mann-Whitney test in GraphPad Prism or by unpaired *t* tests using GraphPad InStat3 software.

RESULTS

Generation of an MA15 mutant panel. The Urbani strain of SARS-CoV was selected for increased pathogenesis after 15 serial passages in 10-week-old BALB/c mice. The resulting mouse-adapted virus, designated MA15, had acquired six amino acid changes in its genome, including mutations in the replicase proteins nsp5, nsp9, and nsp13 and in the S and M structural glycoproteins; this virus caused >20% weight loss and high mortality in mice by 5 days postinfection (dpi) (Fig. 2) (53). To identify mutations that contributed to increased pathogenic outcomes, we created a series of six recombinant viruses, each encoding five of the six mouse-adapted mutations (Fig. 1B). The single-dropout mutant panel was created by sequentially converting each one of the MA15 amino acid changes back to the wild type, using the previously described recombinant MA15 infectious clone (rMA15) (73). The resulting panel of recombinant viruses was designated MA$_{-N5a}$, MA$_{-N5b}$, MA$_{-N9}$, MA$_{-N13}$, MA$_{-S}$, and MA$_{-M}$. The "MA" in each virus designation signifies the MA15 genome; "WT" is used in for the Urbani genome in virus designations. A minus sign or plus sign signifies the addition or deletion of the MA15 mutation at the position identified. "MA$_{-N9}$" means that in the MA15 genome, the nsp9 mutation has been converted back to the WT Urbani amino acid.

After the assembly of full-length molecular clones representing each of the recombinant viruses, full-length transcripts were electroporated into cultures of Vero cells, and recombinant viruses were isolated by plaque assays. Virus stocks were sequenced to
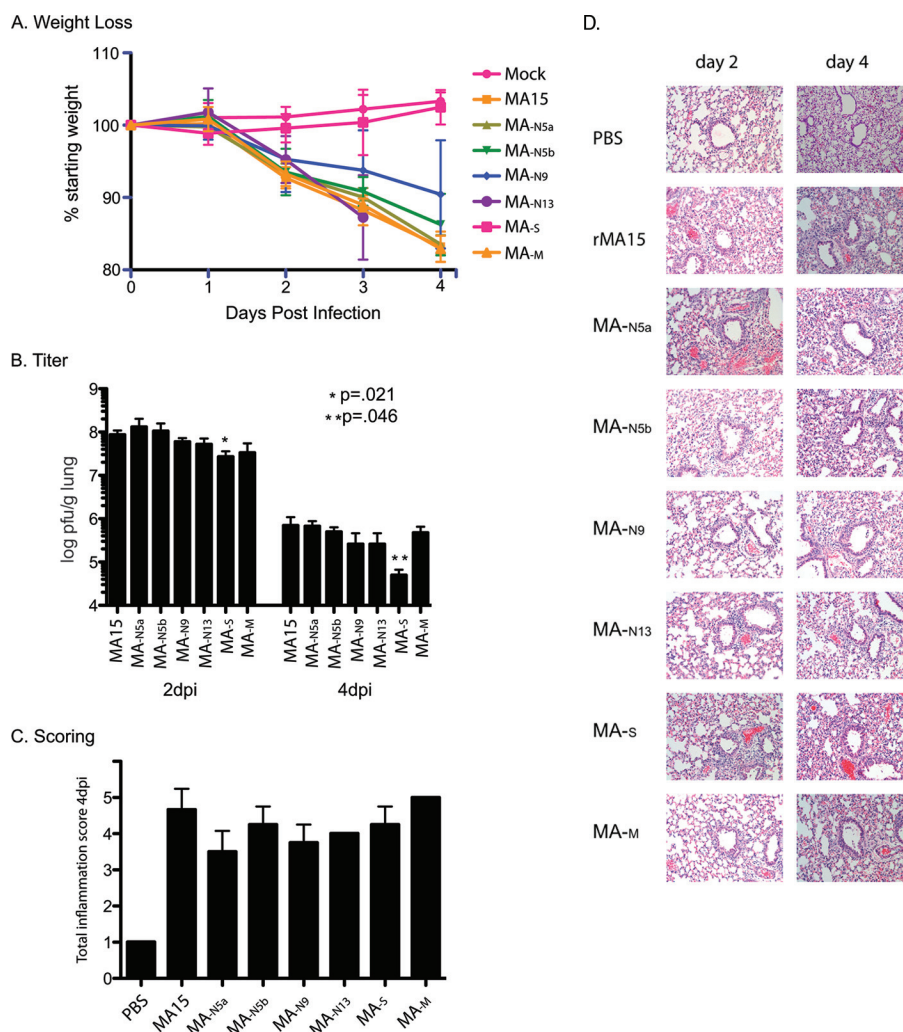
FIG 2 Pathogenesis of rMA15 mutant viruses in young BALB/c mice. (A) Percentages of weight loss for mice infected with rMA15 variant viruses. MA$_{-N9}$- and MA$_{-S}$-infected mice show reductions in weight loss during infection. Ten mice per time point per virus were used. (B) Titers of rMA15 variant viruses at 2 and 4 dpi in the lung. Titers in lung samples were determined on Vero E6 cells. Five experiments were carried out for each virus and time point. (C) Lung sections were stained with H&E and were scored for the amount of inflammation in each section. Scoring was carried out five times for each time point and virus. (D) Images of representative H&E-stained lung sections at 2 and 4 dpi.

verify the existence of appropriate genotypes. The six recombinant virus variants and the wild-type virus were then analyzed for their growth kinetics in Vero E6 cells. Most viruses showed growth kinetics in Vero cells similar to those of the SARS-CoV infectious clone (icSARS) and rMA15, with only MA$_{-M}$ displaying slightly reduced titers 10 to 20 h postinfection (Fig. 1C, left).

Mouse-adapted mutations in the spike protein and nsp9 are required for pathogenesis in young BALB/c mice. To identify alleles associated with pathogenic outcomes, groups of 10-week-old naïve BALB/c mice were inoculated intranasally with 1×10^5 PFU of each MA15 recombinant virus (rMA15) and were then weighed daily (Fig. 2A). In agreement with earlier reports, mice infected with the rMA15 parental virus lost 20% of their starting weight during the 4 days of the infection and showed clinical signs of disease, such as ruffled fur, labored breathing. and malaise. Importantly, mice inoculated with MA$_{-N5a}$, MA$_{-N5b}$, MA$_{-N13}$, or MA$_{-M}$ lost 20% of their body weight over the 4 days of infection. By day 4 postinfection, these mice showed morbidities, such

as ruffling of fur and malaise, comparable to those of rMA15-infected mice. In contrast, animals infected with the MA$_{-N9}$ or MA$_{-S}$ recombinant virus did not develop severe clinical disease or lethal disease outcomes. MA$_{-N9}$-infected mice displayed a variable phenotype, losing 10 to 20% of their starting weight, depending on the mouse. Most did not succumb to infection, suggesting that the mouse-adapted allele in the nsp9 gene may subtly influence severe disease phenotypes. Most importantly, MA$_{-S}$-infected mice uniformly lost less than 5% of their starting weight, showed no visible clinical signs of disease, and did not die. These data suggest that the MA15 allele in the S glycoprotein receptor binding domain (S-RBD) contributed significantly to increased disease in rodents, most likely by enhancing interactions with mouse ACE2 receptors (see Fig. 9). These results are consistent with a large body of data supporting the notion that S glycoprotein-host receptor interactions are a key regulator of emergence, tissue tropism, and species specificity, especially for SARS-CoV and other animal and human coronaviruses (1, 7, 21, 36, 61, 62, 66).

To identify potential correlates of pathogenicity, lungs from infected mice were homogenized, and virus titers were determined on days 2 and 4 postinfection (Fig. 2B). Interestingly, the titers of all mutant viruses were similar to those of rMA15. However, MA_{-S} virus titers were reduced, to a level about 3-fold lower than the rMA15 titer, at day 2 ($P < 0.05$). At 4 days dpi, the differences in replication were more significant, with MA_{-S} displaying a titer 100-fold lower than that of rMA15 ($P < 0.05$). We did not detect any other significant differences in virus titers with the remaining derivative recombinant viruses.

Pathological findings. We have reported a histological analysis of the lungs of mice infected with the rMA15 virus previously (53). We found that mouse lungs displayed rapid progression of inflammation, with extensive damage to the bronchiolar and alveolar epithelial cells. Histological analysis performed with the mutant viruses across the course of infection was compared to our previous findings. After fixation in 4% paraformaldehyde, lungs were sectioned and stained with H&E. Scoring was performed for total inflammation at 4 dpi (Fig. 2C and D). rMA15-infected mice showed increased overall inflammation characterized by peribronchiolar cuffing and a mixed inflammatory infiltrate consisting of neutrophils, eosinophils, and macrophages. The lungs also showed evidence of denuding bronchiolitis, focal alveolitis, focal apoptosis of the airway epithelia, and blockage of the airways with apoptotic debris. Histological analysis of mice infected with the mutant panel showed very similar inflammatory infiltrates and damage to the rMA15 virus. Interestingly, the MA_{-N9} and MA_{-S} viruses displayed no difference in lung pathology from WT MA15 over the course of the infection, even though the mice displayed marked differences in weight loss from rMA15-infected mice. The observation that MA_{-S} exhibited levels of lung pathology similar to those for WT MA15 despite a log reduction in viral titer (Fig. 2B) indicated that other signaling events may be involved in enhancing lung pathology. Similar discrepancies between viral replication and lung pathology have been noted in the pathogenesis of another coronavirus, HC/SZ/61/03 (57).

Dependence on spike and nsp9 mouse-adapted virus mutations for pathogenesis. The data reported above support the hypothesis that the rMA15 pathogenesis phenotype depended heavily on the mutation in the S structural glycoprotein and to a much lesser extent on that in the nsp9 replicase protein. We next examined whether the S and nsp9 mutations were individually sufficient to reproduce the rMA15 pathogenic phenotype in 10-week-old mice. For this purpose, a second panel of derivative isogenic viruses that contained either the MA15 nsp9 mutation or the S glycoprotein mutation alone, designated WT_{+N9} or WT_{+S}, respectively, was constructed on an Urbani virus backbone. We also constructed recombinant viruses containing both the MA15 S and nsp9 alleles (designated $WT_{+N9/S}$) while maintaining the wild-type Urbani alleles at the other four positions. In parallel, a recombinant virus that contained four mouse-adapted mutant alleles but retained the wild-type Urbani alleles in the nsp9 and S proteins (designated $MA_{-N9/S}$) was constructed (Fig. 1B).

Full-length molecular clones were assembled as described previously, and recombinant viruses were produced (73). Each virus was plaque purified and was sequenced to verify the existence of each appropriate genotype. Then the growth of the recombinant viruses in Vero cells was analyzed and was compared to the growth of MA15 *in vitro* (Fig. 1C). These variants showed robust growth, equal to that seen with the rMA15 virus. These data suggest that
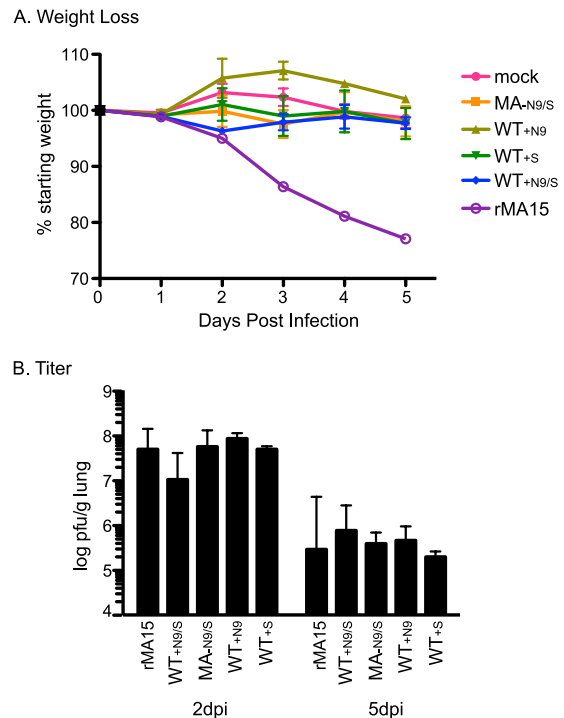

FIG 3 rMA15 nsp9 and spike mutants in young mice. (A) Percentages of weight loss for mice infected with the rMA15 variant viruses diagrammed in Fig. 1B. Note that young mice infected with the nsp9 or S variant show no weight loss, while those infected with rMA15 do. Five experiments were carried out for each virus. (B) Titers of rMA15 variant viruses in the lungs at 2 and 4 dpi. Titers in lung samples were determined on Vero E6 cells. Note that there was no difference between WT and mutant viruses. Five experiments were carried out for each virus.

epistatic interactions across the mutations are minimal *in vitro*, since all recombinant viruses tested replicated efficiently in Vero cells.

The MA15 derivatives were assayed for associated pathogenesis and mortality in 10-week-old BALB/c mice. Groups of mice were inoculated intranasally with a dose of 1×10^5 PFU given intranasally under sedation, as described previously (54). The rMA15 virus produced rapid weight loss, resulting in reductions of >20% of the animals' starting weight by 4 dpi. Like mock-infected controls, mice infected with the $WT_{+N9/S}$, $MA_{-N9/S}$, WT_{+N9}, or WT_{+S} variant failed to lose weight during infection or to show other clinical signs of disease (Fig. 3A). Lungs were analyzed for virus titers, and interestingly, all recombinant virus derivatives showed titers similar to those of the rMA15 virus in the lungs at days 2 and 5 postinfection. Histopathological analysis of the lungs revealed no significant differences from the lungs of mock-infected animals (data not shown). While the MA15 alleles in the S glycoprotein gene and, to a lesser extent, in the nsp9 gene are clearly important contributors to replication and MA15 pathogenesis *in vivo*, as evidenced by the fact that their removal ameliorated the virulence of rMA15, these alleles clearly depend on the presence of one or more additional MA15 mutations in the Urbani virus to cause significant disease in young BALB/c mice.

Immunosenescence differentially modulates the pathogenesis of the MA15 derivative viruses. In humans, age was a major cofactor associated with disease severity following SARS-CoV in-

fection (45, 48). In contrast to young mice infected with a 10^5-PFU dose of SARS-CoV Urbani, 1-year-old mice show a mild clinical disease phenotype that includes ~5% weight loss and increased virus titers, although the animals survive infection (53). Importantly, 1-year-old mice are also significantly more sensitive to rMA15 pathogenicity; rMA15 infection of 1-year-old mice results in increased disease pathology, including pathological findings of acute-phase diffuse alveolar damage characterized by hyaline membrane formation, recapitulating the pathological features commonly noted in human patients infected with SARS-CoV (63). Moreover, the aged-mouse model supports high levels of viral replication. Reasoning that the aged-mouse model would provide a more sensitive measure of the role of individual mutations in virulence and disease outcomes, we compared the replication and pathogenicity of the rMA15 derivatives in 1-year-old mice.

First, we examined the pathogenicity of rMA15 and the previously described MA_{-SM} and WT_{+SM} viruses (Fig. 4A) in 12-month-old BALB/c mice (53). These recombinant viruses carry either the MA15 replicase mutant alleles or the structural glycoprotein S and M mutant alleles, respectively, and do not produce clinical disease and/or death in young (10-week-old) animals (53). With an inoculum of 1×10^5 PFU, all 1-year-old mice demonstrated severe disease by 4 dpi, losing >20% of their starting weight (Fig. 4B). During the course of the infection, all mice showed signs of clinical disease, including ruffling of fur, labored breathing, and lethargy. Lungs were harvested at 2 and 4 dpi for determination of virus titers and histopathological analysis. Importantly, no significant difference in growth between the rMA15, MA_{-SM}, and WT_{+SM} viruses was noted at 2 or 4 dpi in aged BALB/c mice (Fig. 4C). Virus titers in the lung at day 2 approached ~10^8 PFU/g, while day 4 titers were ~10^6 PFU/g.

Lung pathology was analyzed by H&E staining (Fig. 4D). Lungs harvested from mice at 2 and 4 dpi showed pathology similar to that in mice infected with WT MA15 (63). At 2 dpi, lungs showed epithelial cell necrosis, airway debris, and mild peribronchiolar cuffing composed of neutrophils, lymphocytes, and macrophages. At 4 dpi, lungs demonstrated sustained inflammation and inflammatory cell infiltrates with widespread injury of the alveolar parenchyma, interstitial edema with hyaline membranes, and diffuse alveolar damage. Clearly, the attenuated phenotype of the MA_{-SM} and WT_{+SM} viruses seen in young BALB/c mice was not recapitulated in the aged-mouse model, suggesting that fewer and different combinations of MA15 mutations regulate severe disease outcomes in 1-year-old mice.

Lethality of spike and nsp9 mutants in aged mice. In young (10-week-old) BALB/c mice, the MA_{-N9} and MA_{-S} viruses were highly attenuated compared to the MA15 parent strain. Thus, we tested the virulence of these mutants in 12-month-old BALB/c mice with the goal of identifying mutation sets that differentially regulate severe disease outcomes in young and aged mouse models. As previously described, a 1×10^5-PFU inoculum was introduced intranasally into groups of BALB/c mice, and then clinical disease phenotypes were evaluated over the course of infection. We observed that aged mice were as highly susceptible to the MA_{-N9} and MA_{-S} recombinant viruses as they were to the rMA15 virus (Fig. 5A). Animals lost ~20% of their starting weight during the 3 days of infection and were euthanized according to IACUC weight loss criteria. Lungs were harvested at day 3 postinfection due to the severe weight loss of the mice. Minor differences in

A.

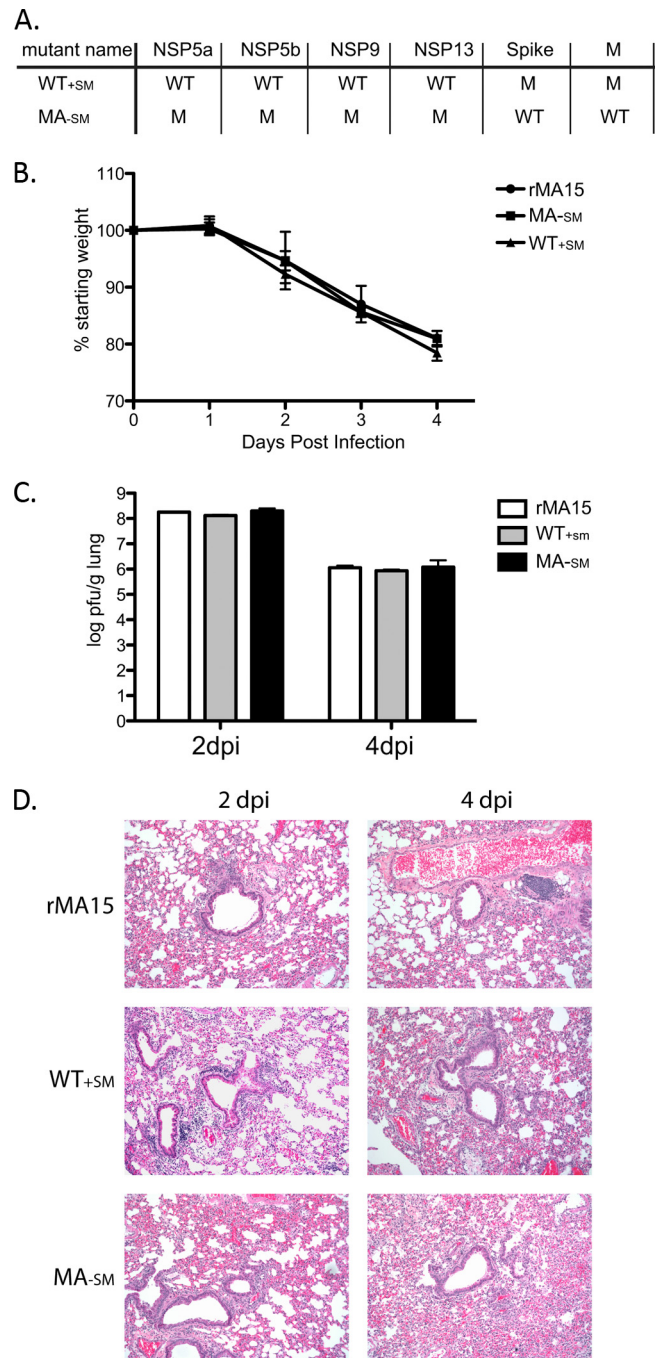| mutant name	NSP5a	NSP5b	NSP9	NSP13	Spike	M
WT+SM	WT	WT	WT	WT	M	M
MA-SM	M	M	M	M	WT	WT

B.

C.

D.

FIG 4 Pathogenesis of rMA15 genome variants in aged mice. (A) Chart showing rMA15 variant viruses encoding only the structural mutations or only the replicase mutations. (B) Percentages of weight loss for mice infected with rMA15 variant viruses. Note that the variants are as pathogenic as rMA15 virus in old mice. Five experiments were carried out for each virus and time point. (C) Titers of rMA15 variant viruses in the lung at 2 and 4 dpi. Titers in lung samples were determined on Vero E6 cells. Note that there was no difference in lung virus titers among the variants and the wild type. Five experiments were carried out for each virus and time point. (D) Images of representative H&E-stained lung sections at 2 and 4 dpi. Note the high levels of eosinophil and neutrophil infiltration in the lungs of infected mice.
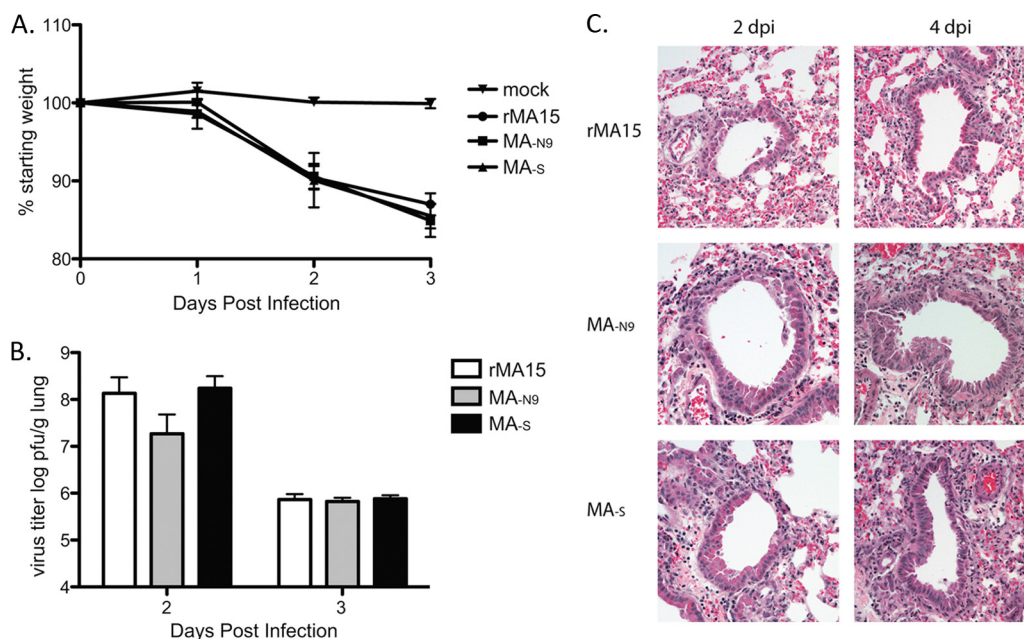
FIG 5 MA15 S and nsp9 variant viruses in aged mice. (A) Percentages of weight loss for mice infected with MA15 variant viruses. Aged mice infected with the MA$_{-N9}$ or MA$_{-S}$ virus display weight loss similar to that with rMA15. Five experiments were carried out for each virus and time point. (B) Titers of rMA15 variant viruses in the lung at 2 and 3 dpi. Titers in lung samples were determined on Vero E6 cells. Note that there was little difference in lung titers among the variants and the wild type at either 2 or 3 dpi. Five experiments were carried out for each virus and time point. (C) Images of representative H&E-stained lung sections at 2 and 3 dpi. Notice the high levels of inflammation and infiltration in these lungs. Airways display continued inflammation throughout the infection.

titers were found, but these differences were not statistically significant ($P > 0.05$) (Fig. 5B). The histological findings did not differ significantly from those for the parent virus (Fig. 5C). The predominant pathological feature was denuding bronchiolitis with accumulation of debris in the airways. Inflammatory infiltrates (e.g., neutrophils, macrophages, lymphocytes) surrounded and penetrated the airway epithelium, and perivascular cuffing was prominent. The lung parenchyma displayed focal inflammatory foci consisting of neutrophils and eosinophils with alveolar thickening and overall high levels of cellularity. Hyaline membranes and diffuse alveolar damage were evident. We conclude that MA$_{-SM}$, WT$_{+SM}$, MA$_{-N9}$, and MA$_{-S}$ variants are also fully virulent in the 1-year-old mouse model, demonstrating that different combinations of mouse-adapted mutations recapitulate severe disease outcomes in the lung that are seen following infection in humans (45). Together, these results suggest that most mouse-adapted mutations enhance intrinsic pathogenic properties encoded in the viral genome and that aged mice differ from young mice in their ability to respond to, and induce protection from, viruses that are attenuated in young mice.

The spike and nsp9 mutations together are necessary and sufficient to regulate pathogenesis in aged mice. We next evaluated the role of the mouse-adapted nsp9 and S mutations in age-related disease outcomes. The viruses used contain reciprocal combinations of S and nsp9 mutations in either the Urbani or the MA15 background.

We compared the pathogenicity of WT$_{+N9/S}$, MA$_{-N9/S}$, WT$_{+N9}$, and WT$_{+S}$ in aged mice (viruses described in Fig. 1B). As described previously, 12-month-old BALB/c mice were inoculated with 1×10^5 PFU of each virus, and clinical disease outcomes were evaluated daily. In young BALB/c mice, all of these mutants were attenuated. However, in aged mice, disease phenotypes differ with each mutant (Fig. 6A). In comparison to the effects of rMA15 on 12-month-old BALB/c mice, SARS-CoV Urbani causes 5% weight loss, grows to a lower titer in the lungs, and causes mild inflammation. The mutant viruses WT$_{+N9/S}$ and MA$_{-N9/S}$ caused significant weight loss and death in 1-year-old mice. Comparatively, recombinant virus WT$_{+N9}$ or WT$_{+S}$ caused only mild weight loss and clinical disease. Importantly, WT$_{+S}$ did cause some mortality (2/8 mice), especially when the experiment was extended through 7 days. The titers of rMA15 and MA$_{-N9/S}$ in lungs at 4 dpi were similar, while WT$_{+N9/S}$, WT$_{+N9}$, and WT$_{+S}$ demonstrated >10-fold-higher titers (Fig. 6B). Histological analysis was performed on the lungs of these mice, and only slight differences between the strains were noted; the lungs displayed pathological features described previously for aged mice (55) (Fig. 6C). Interestingly, MA$_{-N9/S}$ showed a tendency toward greater hyaline membrane formation, although this was not a statistically significant difference (Fig. 6C). Additionally, WT$_{+N9}$ displayed focal eosinophilia at a frequency slightly (but, again, not statistically significantly) higher than those for the other mutants. These data further demonstrate that the S and nsp9 mutations together, as seen in WT$_{+N9/S}$, or in combination with the other four mouse-adapted mutations, are sufficient to cause disease similar to that caused by rMA15 in aged mice. However, when the S and nsp9 mutations are the sole mutations in the SARS-CoV genome, the mutants are significantly less virulent in old mice, suggesting that there are unique virus-host interactions in old mice with the other MA15 mutations that are important for disease progression and pathogenesis.

We next infected 12-month-old mice with varying amounts of each MA15 derivative virus so as to better identify unique pathogenic phenotypes for each of the mutant viruses. Mice were infected with WT$_{+N9/S}$, MA$_{-N9/S}$, or WT$_{+S}$ at doses of 1×10^2 PFU,
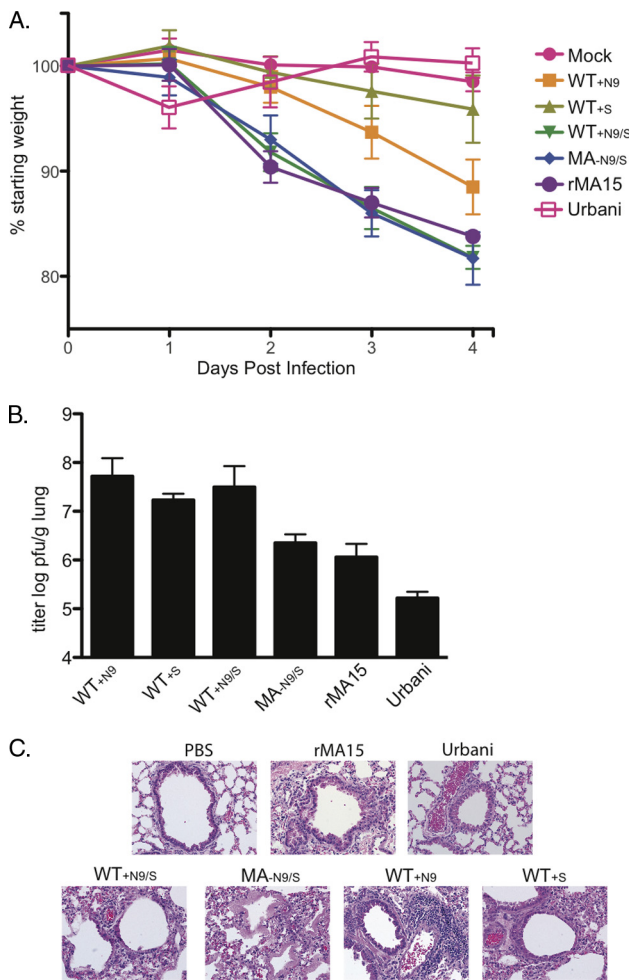
FIG 6 MA15 S and nsp9 combination variant viruses in aged mice. (A) Percentages of weight loss of mice infected with rMA15 variant viruses. Aged mice infected with $WT_{+N9/S}$ or $MA_{-N9/S}$ display weight loss similar to that with rMA15. Five experiments were carried out for each virus. (B) Titers of virus in the lungs at 4 dpi were normal for $MA_{-N9/S}$ and WT_{+N9}, while WT_{+S} and $WT_{+N9/S}$ demonstrated >1-log-lower titers. Five experiments were carried out for each virus and time point. (C) Images of representative H&E-stained lung sections at 4 dpi.

1×10^3 PFU, 1×10^4 PFU, or 1×10^5 PFU per mouse. With rMA15, a dose of 1×10^2 PFU is fully pathogenic and virulent in aged mice; the mean day of death is day 5.4 ± 0.54 (Fig. 7A and Table 1). In contrast, the mutant viruses $WT_{+N9/S}$ and $MA_{-N9/S}$ were significantly less virulent at a low dose (1×10^2 PFU/mouse), and all mice survived infection. However, after high-dose infection (1×10^5 PFU/mouse), the $WT_{+N9/S}$ and $MA_{-N9/S}$ derivative mutants were as lethal as rMA15. Importantly, WT_{+S}, which contains only the mouse-adapted S mutation, also was not lethal at low doses; however, inoculation with 1×10^5 PFU per mouse resulted in some lethality. Interestingly, the 50% lethal doses (LD_{50}) for the $WT_{+N9/S}$ and $MA_{-N9/S}$ viruses were higher than that for rMA15 (Table 1). This observation indicated that although the nsp9 mutation and especially the S mutation are important contributors to pathogenicity in old mice, additional MA15 mutations are needed to enhance disease progression and death. A recent report by Ebihara et al. identified a similar increase

in the LD_{50} in a derivative panel of mouse-adapted Ebola viruses, where the variant containing mouse-adapted mutations in the nucleoprotein (NP) and viral protein 24 (VP24) could still cause lethality, but the LD_{50} was increased 5-fold (11). These observations together indicate that although key mouse-adapted mutations alone could impart lethality, a complete set of mouse-adapted mutations collectively regulate pathogenesis.

We conclude that while highly attenuated in young mice, the rMA15 viruses with both nsp9 and S MA15 mutant alleles are capable of causing severe disease outcomes and death in aged mice. Viruses with only the nsp9 mutant allele are not fully virulent in 1-year-old mice, while the virus with only the S MA15 mutant allele is still moderately pathogenic in 1-year-old mice, especially at higher doses. These data suggest that the expression or functional activity (e.g., senescence) of one or more cellular factors mediates differential disease outcomes in young and aged mice.

Novel mouse-adapted SARS-CoVs produce similar disease in mice. Our data indicated that host senescence significantly enhanced the virulence of rMA15 and the derivative recombinant virus panel, in agreement with the pathological phenotypes seen in human SARS-CoV infections. Mouse adaptation may enhance intrinsic pathogenic properties encoded in the SARS-CoV and/or evolve new virus-host interactions and signaling networks that promote disease severity. Because the analysis of each of these SARS-CoV mutants depends on the initial identification of a mouse-adapted strain of the virus, we wanted to determine whether this mouse-adapted strain was unusual in its adaptation. For this purpose, we isolated an additional mouse-adapted strain of SARS-CoV, designated MA20, and determined whether similar adaptive mutations had evolved after independent selection and/or produced similar disease outcomes in young and aged animals. MA20 was mouse adapted after 20 independent serial blind passages at 2-day intervals in 10-week-old BALB/c mice and encoded six amino acid changes that were associated with increased virulence. Day et al. have also recently published the sequence of a novel mouse-adapted strain of SARS-CoV, called v2163 (8). Strain v2163 was isolated from the serial passage of SARS-CoV Urbani in 6-week-old BALB/c mice and contains 10 amino acid changes in its genome. Comparing the 3 independently isolated mouse-adapted viruses, we found mutated genes common to all 3 (nsp13, Spike), mutated genes common to 2 of the 3 viruses (nsp5, M), and genes that were mutated in only a single virus (nsp3, nsp14, 3b/E) (Fig. 8A). First, an identical M glycoprotein mutation (E11K) evolved in both the MA15 and MA20 mouse-adapted viruses. Remarkably, the S-RBD contained a series of related and unique mutations in all three strains. The mutations clustered at the interface between the RBD and the ACE2 receptor and are predicted to affect RBD interaction with the orthologous mouse ACE2 receptor used for docking and entry (Fig. 8 and 9). In addition, both MA15 and v2163 have evolved mutations in nsp9 that localize at different but nearby positions. These clustered mutations support the hypothesis of a role for these genes in mouse adaptation and disease potential, especially in young animals.

To compare disease outcomes with the three mouse-adapted viruses, we infected 10-week-old BALB/c mice with 1×10^5 PFU each, or with PBS as a control, and weighed the mice daily (Fig. 8B). All three viruses caused similar weight loss kinetics during the experiment: the mice lost >20% of their starting weight over the 4 days of infection. Lungs were dissected from mice at 2 and 4 dpi,
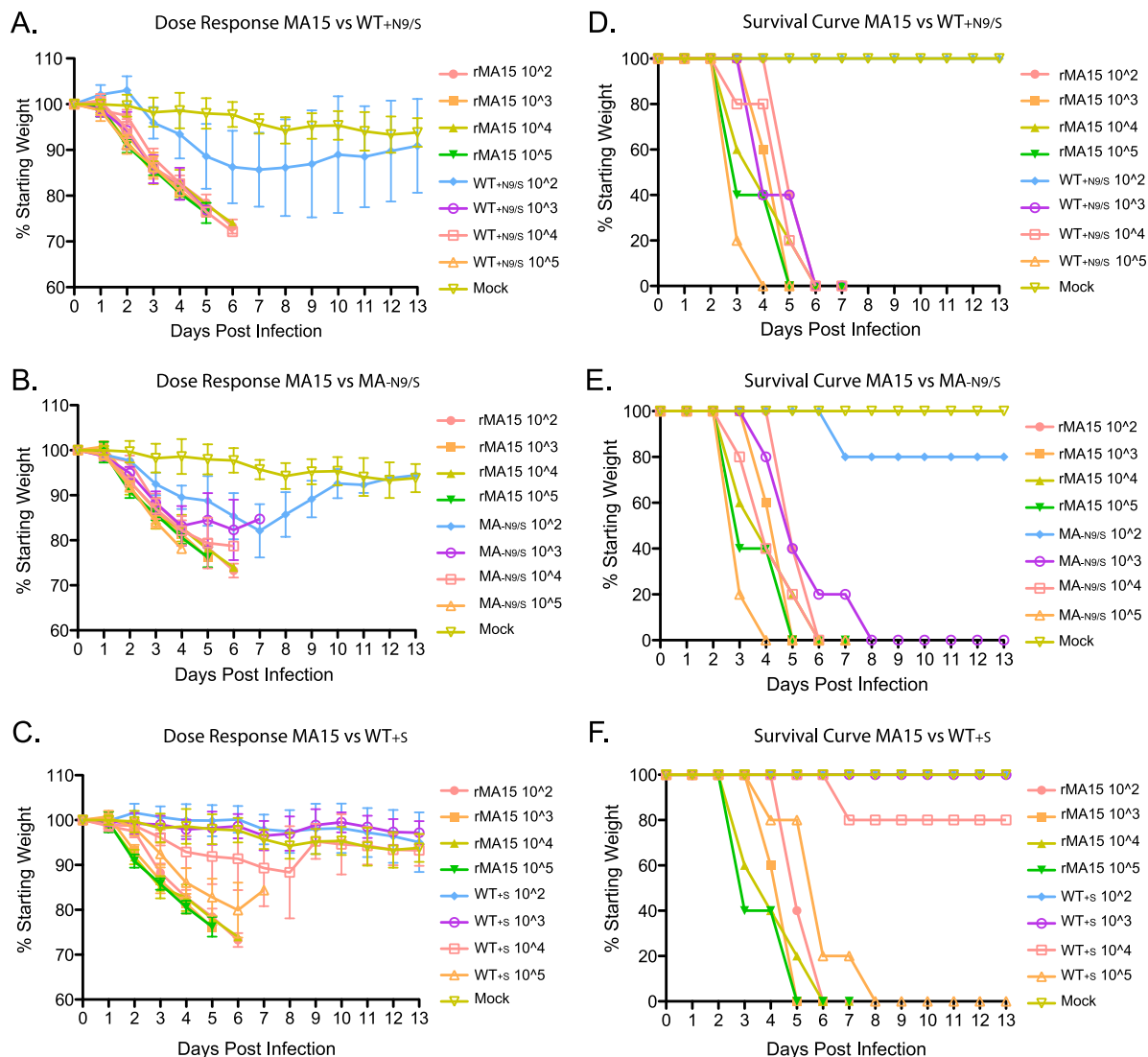
FIG 7 (A to C) Dose-response curves of rMA15 variant viruses in aged mice. WT MA15, as well as WT$_{+N9/S}$ (A), MA$_{−N9/S}$ (B), and WT$_{+S}$ (C), was used to infect aged mice with different doses of virus. (D to F) Survival curves are plotted alongside each dose-response curve. Five experiments were carried out for each virus.

and viruses were quantified by plaque assays (Fig. 8C). No significant differences in virus titer were noted following infection with the three mouse-adapted viruses at either day 2 or day 4 postinfection. MA20 caused disease pathology similar to that caused by MA15 and v2163, revealing no significant differences in lung pathology between the three strains (data not shown). These data support the hypothesis that common mutations allowing for increased pathogenicity and disease in a host are acquired in the SARS-CoV, and they suggest that important virus-host interactions occur during infection.

DISCUSSION

Virus passage *in vivo*, and mouse adaptation in particular, is a common strategy used to develop robust animal models for human disease (e.g., Ebola virus [11], Marburg virus [5], hantaviruses [4, 28, 35], respiratory syncytial virus [RSV] [24], human coronaviruses [32, 53], dengue virus [64, 65], yellow fever virus [15]), poliovirus [31], and influenza virus [27]). This necessary

step reflects basic findings that many viruses cause significant disease outcomes in humans but mild or minimal clinical disease and pathology in rodents. While potentially complicating comparisons across mouse and human species, mouse-adapted viruses afford access to a wealth of reagents developed for the laboratory mouse, including access to genetically defined mutants. In this study, we use a reverse genetic approach to identify the genetic determinants of mouse-adapted SARS-CoV that regulate virulence in young and 1-year-old mice. Three mouse-adapted strains of SARS-CoV (MA15, v2163, and MA20) have now been independently isolated and reported in the literature. Among these, the pathogenesis of MA15 has been extensively studied by transcriptomics and disease outcomes in genetically defined knockout mice and in young and aged mouse models of human disease (17, 53, 60, 74, 75), providing considerable insight into key virus-host interactions that differentially regulate disease processes and pathogenic outcomes following infection. More recently, transgenic mice expressing the human ACE2 receptor used by SARS-CoV for

TABLE 1 Fifty percent lethal dose and mean day of death for 1-year-old female BALB/c mice infected intranasally with the indicated dose of virus[a]

Virus and dose	LD_{50}	Mean day of death
MA15	$<10^2$	
10^2		5.4 ± 0.54
10^3		4.6 ± 0.54
10^4		4.2 ± 1.3
10^5		3.8 ± 1.09
WT$_{+N9/S}$	$10^{2.5}$	
10^2		NA[b]
10^3		4.4 ± 0.54
10^4		4.8 ± 1.09
10^5		3.2 ± 0.44
MA$_{-N9/S}$	$10^{2.3}$	
10^2		NA
10^3		5.6 ± 1.51
10^4		4.4 ± 1.14
10^5		3.2 ± 0.4
WT$_{+S}$	$10^{4.375}$	
10^2		NA
10^3		NA
10^4		NA
10^5		6 ± 1.26

[a] Viruses used were the mouse-adapted SARS-CoV (MA15) and mutant derivatives of MA15 and wild-type SARS-CoV Urbani. For each dose of each virus, five animals were infected.
[b] NA, not applicable.

virus docking and entry have provided an alternative approach for developing mouse models of SARS-CoV pathogenesis (39), although these mice also develop a lethal neurologic disease, which is rarely seen in human SARS patients. While both approaches provide considerable insight into the molecular mechanisms governing virus pathogenesis (e.g., poliovirus [52] and measles virus [22, 51]), few models are available that simultaneously compare and contrast mutation spectra after cross-species transmission from animals to humans (wild-type SARS-CoV from bats and civets) and from humans to animals (human viruses to mouse-adapted viruses) and the development of severe disease outcomes. Moreover, few studies have sequentially reisolated mouse-adapted strains to identify the spectrum of shared and unique molecular determinants that regulate host adaptation and disease phenotypes in young and/or aged animal models of human disease.

Most human coronaviruses replicate poorly in mice, resulting in the selection of mouse-adapted strains for pathogenesis studies in small animals (OC43 and 229E) (3, 26, 32). SARS-CoV is a highly pathogenic respiratory coronavirus that emerged from zoonotic sources in China in 2003, providing a unique opportunity to compare and contrast the molecular determinants that regulate virus evolution, adaptation, and virulence in new species by using humans and mice as models. Importantly, the epidemic strain of SARS-CoV (the Urbani strain) replicates and produces minimal disease in mice; however, this provides an opportunity to model, compare, and contrast the evolution of virulence-enhancing mutations in rodent and human hosts. In this capacity, we sought to identify the mutations that are necessary and suffi-

cient to cause the lethal disease produced by MA15, enabling us to elucidate the important molecular determinants regulating virus-host interaction and virulence in young and aged animal models of human disease.

Infection with MA15 mutants, each lacking one change in the parental mouse-adapted virus, demonstrated that mutations in the replicase nonstructural protein nsp9 and the spike glycoprotein contributed to increased SARS-CoV pathogenesis in young mice (Fig. 2 and 5). Attesting to the importance of these proteins in viral pathogenesis, other, independently derived mouse-adapted SARS-CoV strains also displayed mutations in these genes, as evidenced by nsp9 mutations in MA15 and v2163 and S-RBD mutations that emerged in all three mouse-adapted strains (Fig. 7A). To further our understanding of the role of these mutations in pathogenesis, we introduced the nsp9 and S mouse-adapted virus mutations into icSARS (Urbani) either singly or in combination. In young animals, recombinant viruses with either the single or double mutations at these positions replicated to higher titers but did not produce more-severe clinical disease than did the wild-type virus (Fig. 3A and B). These data suggest that the mutation in the S glycoprotein plays a prominent role, while the influence of the nsp9 mutation is more variable. The mutations, alone or in combination, are necessary but not sufficient to cause disease in young mice. In agreement with this hypothesis, independent generation of three mouse-adapted SARS-CoVs resulted in mutations in genes encoding the M glycoprotein and the replicase protein nsp13. Two of three mouse-adapted viruses also contained mutations in nsp5 (Mpro) (Fig. 8A), and sporadic mutations were identified in either nsp3 or nsp14. Among these mutations, previous studies had suggested that a mutation at position 11 (E11K) in the MA15 M glycoprotein gene enhanced virus yields in cells, suggesting a key role in improving the efficiency of virus maturation and release in different hosts (46). Mutations in the mouse hepatitis virus (MHV) nsp14 gene, encoding a putative RNA proofreading function and 7-0-methyltransferase, were also shown to attenuate pathogenesis in mice, supporting the role of nsp14 as a putative virulence allele (9, 13, 50, 68). It is noteworthy that mutations in the S and M glycoprotein genes were also observed during cross-species transmission of SARS-CoV to humans, suggesting commonalities in the regulation of virulence in the two species. Other mutations associated with the emergence of human disease also evolved in the ORF1a nonstructural proteins nsp1, nsp2, and nsp3, as well as in the ORF1b nonstructural proteins nsp13, nsp14, and nsp15 (7). Although the sites are different, mutations in nsp3, nsp13, and nsp14 also evolved during mouse adaptation. Similar observations have been noted in mouse-adapted Ebola virus, where a combination of mutations in NP and VP24 is essential for lethality in young BALB/c mice, though none of these individual mutations alone could impart pathogenicity (11). Based on precedents from other systems, likely functions of these mutations may be to enhance virus replication in mice, engage host innate immune signaling networks, influence RNA fidelity rates, and/or ablate interferon-stimulated antiviral gene activities (9, 12, 16, 34, 41).

The mouse ACE2 receptor interacts weakly with epidemic (Urbani) strain S glycoprotein RBDs in vitro in biochemical studies and in studies with pseudotyped viruses (71, 72) (modeled in Fig. 9). This is most likely because a K353H difference in mACE2 remodels the interactions between residues D38, Q42, and H353 of mACE2 and residue Y436 of the Urbani RBD, the bulky aromatic
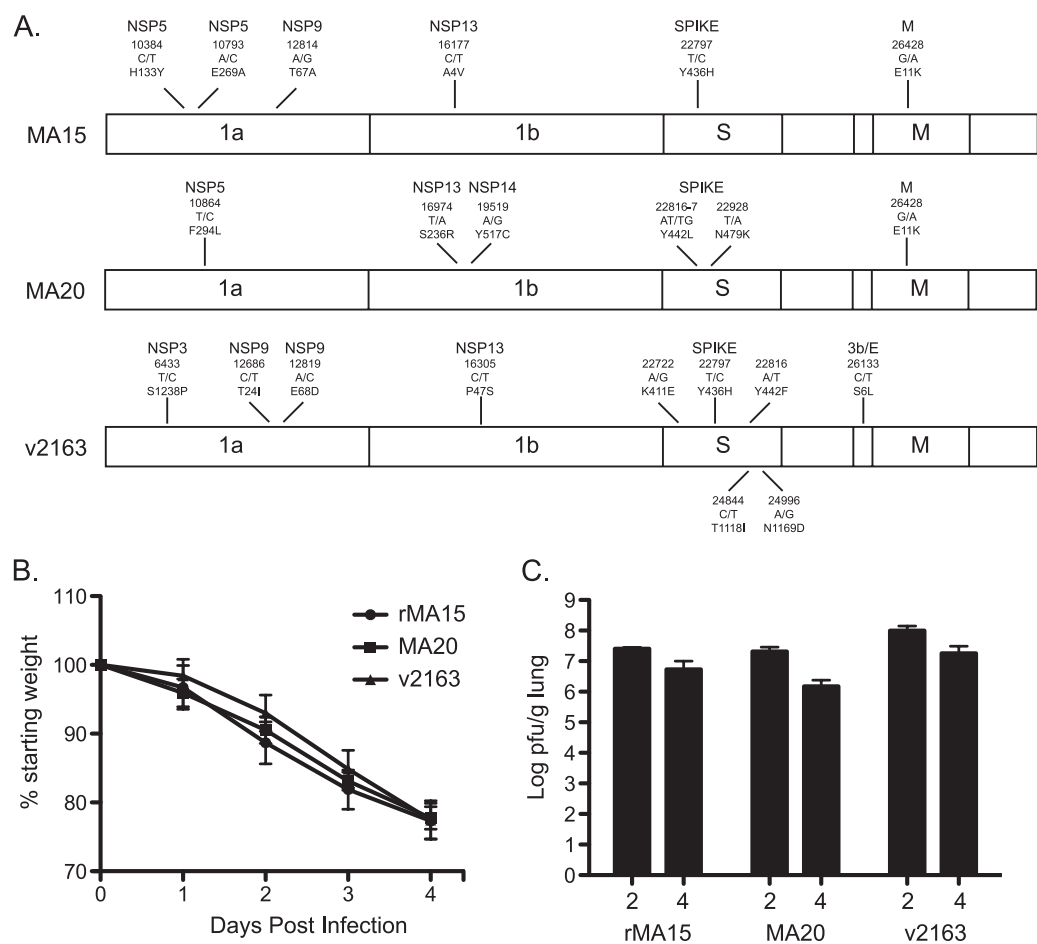
FIG 8 Comparative pathogenesis of three mouse-adapted SARS-CoVs. (A) Schematic of mutation differences among rMA15, MA20, and v2163. (B) Weight loss curves for young mice infected with MA15, MA20, or v2163. Five experiments were carried out for each virus. (C) Virus titers in the lungs of mice infected with rMA15, MA20, or v2163 at 2 and 4 dpi. Five experiments were carried out for each virus and time point.

side chain of which potentially reduces binding. Mutation of His353 to K in mACE2 allows more-efficient infectivity of SARS-CoV for murine cells (36). In accordance with our understanding of coronavirus-receptor interactions and host range, mutations in the RBD of the S glycoprotein were positively selected during the adaptation of MA15, MA20, and v2163 to mice and during zoonotic-strain adaptation to humans. As was predicted during the human epidemic, modeling studies strongly support the hypothesis that these three unique mutation sets enhance viral S-RBD interaction with the mACE2 receptor, primarily by allowing for efficient recognition of D38 or a polar region established by mACE2 N30, N31, and Q34 at the viral S-RBD–ACE2 interface (Fig. 9). Previous studies have identified 13 contact residues in the SARS-CoV RBD, including residue Y436, which interacts with ACE2 residues D38 and Q42, sites that are identical in the mouse and human receptors (40, 71). Of note, the K353H difference in mACE2 also contributed to this remodeling, since this change likely allowed D38 to interact with H436 more efficiently. In contrast, MA20 evolved changes at Y442L and N479K in the RBD, which likely form polar interactions with two asparagine residues at positions 30 and 31 of mACE2. In addition, the Y442L change in the MA20 RBD removes the bulky aromatic side chain of tyrosine, allowing K479 of the MA20 RBD access to binding partners N30

and N31 of mACE2. Finally, v2163 evolved the K411E, Y436H, and Y442F mutations in the RBD. Structural modeling suggests that v2163 encodes adaptations that target both sites that adapted in MA15 and MA20. The observation that v2163 optimized binding to two sites on mACE2 suggests that v2163 may have a higher binding affinity for the mACE2 receptor than MA15 and/or MA20, a feature that may have been required for enhancing pathogenesis in 6-week-old mice. Structural and biochemical studies will be needed to confirm these models.

The emergence of several unique evolutionary pathways that enhance mACE2 usage attests to the flexibility of the RBD-ACE2 interface, in agreement with earlier studies in our laboratory, which identified several mutation pathways that promote the recognition of the hACE2 receptor by civet strain SZ16 (62). Of note, mutations in the RBD of the S glycoprotein of MA15 were absolutely essential for enhanced pathogenesis in young animals. These data are also consistent with earlier studies in our laboratory that demonstrated that recombinant isogenic SARS viruses encoding early human and civet S glycoproteins led to enhanced disease in aged mice (56). Surprisingly, some of the MA15 molecular determinants that regulated enhanced virulence and pathogenesis in aged animals were overlapping while others were unique, supporting earlier hypotheses that host factors played a
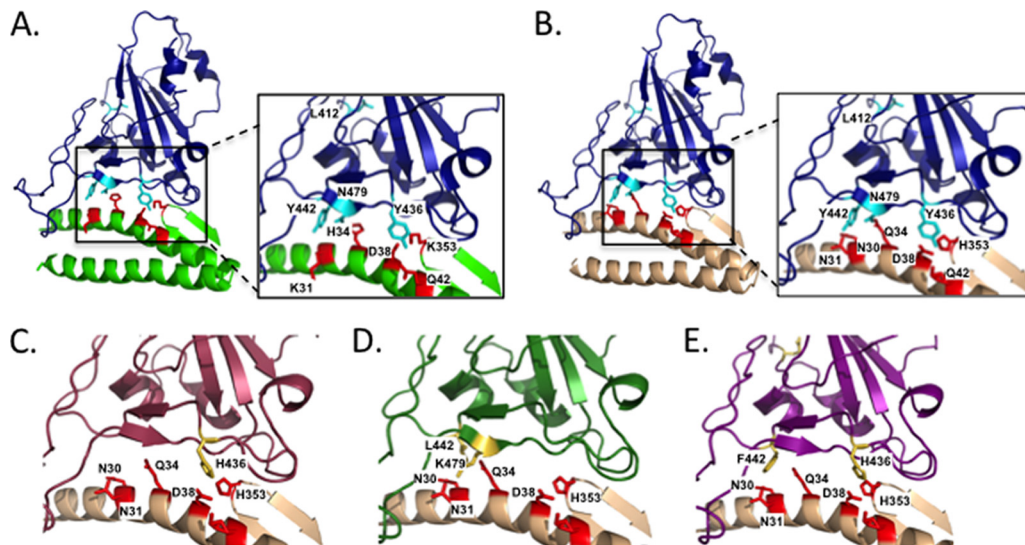
FIG 9 Structural comparison of mouse-adapted SARS-CoV mutations and ACE2. (A) Interactions between the Urbani RBD (blue) and human ACE2 (green). The residues in the RBD that change during adaptation to mouse ACE2 are highlighted (cyan). The human ACE2 residues that interact with those RBD sites are shown in red. A key electrostatic interaction occurs between D38 and K353 of human ACE2 (weakened in mouse ACE2). (B) Interactions between the Urbani RBD (blue) and mouse ACE2 (tan). The residues in the RBD that change during adaptation to mouse ACE2 are highlighted (cyan). The mouse ACE2 residues that likely interact with those RBD sites are shown in red. (C) Adaptation of MA15 to mACE2. The Y436H change allows MA15 to interact more robustly with mACE2, since Y436H likely increases binding via electrostatic interaction with D38 of mouse ACE2. Purple, MA15 RBD; tan, mouse ACE2; yellow, residue that changed in MA15; red, residues interacting with RBD sites that adapted to mACE2. (D) Adaptation of MA20 to mACE2. The Y442L and N479K adaptations allow these residues to interact with N30, N31, and Q34 of mACE2, likely increasing binding affinity. MA20 K479 can bind to both N30 and N31 of MA20 via polar interactions, and MA25 L442 likely interacts with Q34 of mACE2. Green, MA20 RBD; tan, mouse ACE2; yellow, residue that changed in MA20; red, residues interacting with RBD sites that adapted to mACE2. (E) Adaptation of MA25 to mACE2. As with MA15, the Y436H change likely allowed this residue to interact more robustly with D38 of mACE2, with the K353H difference in mACE2 playing a key role. In addition, the Y442F adaptation removes a hydroxyl group from the binding interface, likely mediating a better fit between MA25 and mACE2. Purple, MA25 RBD; tan, mouse ACE2; yellow, residue that changed in MA20; red, residues interacting with RBD sites that adapted to mACE2.

critical role in regulating SARS-CoV virulence and pathogenic outcomes (17, 56, 63, 75).

SARS-CoV produced asymmetric disease outcomes in young and 1-year-old animals, as evidenced by increased virus titers, more-severe disease outcomes, reduced LD_{50} values, and higher mortality rates in aged populations; similar results have been reported for humans >65 years of age (29). Fatal and severe disease outcomes for the elderly have also been reported with other human coronaviruses, such as OC43 (47). The molecular mechanisms governing age-related disease susceptibility are unclear but have generally been linked to a progressive age-related senescence of the immune system and perhaps other key cellular activities that participate in virus-host interactions and disease (56). Studies reported here and previously clearly demonstrate that SARS-CoV and MA15 virulence and pathogenesis are exquisitely sensitive to aging processes in humans and mice, and in contrast to other mouse models of immunosenescence, virulence is clearly visible in 1-year-old mice. In rMA15 infection of aged versus young mice, the LD_{50} drops from ~10^4 to 10^2 PFU and from >10^6 to 10^2 PFU for the BALB/c and C57BL/6 strains, respectively (63). In young mice, pathological changes include acute denuding bronchiolitis, perivascular cuffing, and mild alveolitis. In contrast, aged animals display similar but more-severe airway and vascular changes, including more severe-cuffing and pneumonia with neutrophils, macrophages, lymphocytes, and scattered eosinophils, diffuse alveolar damage, and hyaline membranes, symptoms that are prominent in severe human infection. Additionally, we observed an interesting difference in pathogenesis among the mutant vi-

ruses in young mice. MA_{-S} produced virus titers and lung pathology equal to those produced by the other single mutant viruses but did not induce weight loss in young mice. We hypothesize that the interaction of the mouse-adapted spike protein with its mACE2 receptor may alter the signaling and host response from those with human ACE2, leading to the differences in virus titer and weight loss. Further experiments are needed to follow up this hypothesis.

Finally, virulence in young animals appears to require the coordinated evolution of 6 to 10 mutations, including critical genetic determinants in the S glycoprotein that are likely augmented by mutations encoded elsewhere in the genome. In contrast, the S glycoprotein mutation alone, as well as many different combinations of the other mutations, produced lethal disease outcomes in 1-year-old mice. To our knowledge, comparative pathogenesis of mouse-adapted viruses as a function of age has not been demonstrated previously in the literature. Disease patterns in aged mice replicated pathological outcomes and clinical disease symptoms seen following infection with the MA15 parent virus. These phenotypes included similar virus titers and increased lung pathology, mimicking the severe disease phenotypes seen during human infections in aged, but not young, populations. These data clearly demonstrate that different viral determinants influence pathogenic outcomes in young and aged mouse populations.

Molecular determinants have been precisely mapped for many mouse-adapted viruses, yet MA15 is unique in that several overlapping and/or completely different sets of mouse-adapted mutations produce lethal disease outcomes in aged, but not young, animals. These outcomes could be explained by the presence of

different sets of mutations that differentially influence virus replication and/or host signaling networks in young and aged animals. Alternatively, these mutations may simply increase viral replication and thereby enhance the effect of intrinsic virulence determinants encoded in the SARS-CoV genome. These effects can be further enhanced as a result of immunosenescence and aging of the host. Dissection of the host response pathways that differentially regulate the disease outcome in young and aged populations not only would shed light on host-pathogen interactions important during SARS-CoV infection of humans but may also identify early markers of immunosenescence. Detailed genomic analyses of recombinant viruses containing the mouse-adapted nsp9 or S mutation alone or with other alleles will also be essential for dissecting the roles of these mutations in pathogenesis.

We have mapped the molecular determinants in mouse-adapted SARS-CoV that recapture human disease phenotypes and age-related disease outcomes, including enhanced lung pathology. We have also shown that the mutations work in concert and are critical for the disease progression of SARS-CoV in both young and old mouse models. Experiments with passage of SARS-CoV Urbani showed the evolution of genes (nsp5, nsp13, M, and S) that were also shown to evolve during the emergence of SARS-CoV from animal reservoirs. We postulate that comparison of the host signaling and transcriptional profiles of viruses causing either attenuated or lethal disease will identify signatures associated with outcomes in both mice and humans. We demonstrate that SARS-CoV pathogenesis is exquisitely sensitive to host immunosenescence, recapitulating the disease burden seen in humans. Moreover, our model system may provide a unique probe for the identification of early markers of immunosenescence or of broad regulators of progressive senescence in innate and adaptive immune and respiratory function. Identification of the molecular mechanisms governing SARS-CoV disease in immunosenescence may provide considerable opportunities for ameliorating the increased disease burden associated with infections in the elderly.

ACKNOWLEDGMENTS

REFERENCES

1. **Babcock GJ, Esshaki DJ, Thomas WD, Jr, Ambrosino DM.** 2004. Amino acids 270 to 510 of the severe acute respiratory syndrome coronavirus spike protein are required for interaction with receptor. J. Virol. **78:** 4552–4560.
2. **Barretto N, et al.** 2005. The papain-like protease of severe acute respiratory syndrome coronavirus has deubiquitinating activity. J. Virol. **79:** 15189–15198.
3. **Barthold SW, de Souza MS, Smith AL.** 1990. Susceptibility of laboratory mice to intranasal and contact infection with coronaviruses of other species. Lab. Anim. Sci. **40:**481–485.
4. **Botten J, et al.** 2000. Experimental infection model for Sin Nombre hantavirus in the deer mouse (*Peromyscus maniculatus*). Proc. Natl. Acad. Sci. U. S. A. **97:**10578–10583.
5. **Bray M.** 2001. The role of the type I interferon response in the resistance of mice to filovirus infection. J. Gen. Virol. **82:**1365–1373.
6. **Cheung OY, Chan JW, Ng CK, Koo CK.** 2004. The spectrum of pathological changes in severe acute respiratory syndrome (SARS). Histopathology **45:**119–124.
7. **Chinese SARS Molecular Epidemiology Consortium.** 2004. Molecular evolution of the SARS coronavirus during the course of the SARS epidemic in China. Science **303:**1666–1669.
8. **Day CW, et al.** 2009. A new mouse-adapted strain of SARS-CoV as a lethal model for evaluating antiviral agents in vitro and in vivo. Virology **395:**210–222.
9. **Denison MR, Graham RL, Donaldson EF, Eckerle LD, Baric RS.** 2011. Coronaviruses: an RNA proofreading machine regulates replication fidelity and diversity. RNA Biol. **8:**270–279.
10. **Drosten C, et al.** 2003. Identification of a novel coronavirus in patients with severe acute respiratory syndrome. N. Engl. J. Med. **348:**1967–1976.
11. **Ebihara H, et al.** 2006. Molecular determinants of Ebola virus virulence in mice. PLoS Pathog. **2:**e73.
12. **Eckerle LD, et al.** 2010. Infidelity of SARS-CoV Nsp14-exonuclease mutant virus replication is revealed by complete genome sequencing. PLoS Pathog. **6:**e1000896.
13. **Eckerle LD, Lu X, Sperry SM, Choi L, Denison MR.** 2007. High fidelity of murine hepatitis virus replication is decreased in nsp14 exoribonuclease mutants. J. Virol. **81:**12135–12144.
14. **Egloff MP, et al.** 2004. The severe acute respiratory syndrome-coronavirus replicative protein nsp9 is a single-stranded RNA-binding subunit unique in the RNA virus world. Proc. Natl. Acad. Sci. U. S. A. **101:**3792–3796.
15. **Fitzgeorge R, Bradish CJ.** 1980. The in vivo differentiation of strains of yellow fever virus in mice. J. Gen. Virol. **46:**1–13.
16. **Frieman M, Ratia K, Johnston RE, Mesecar AD, Baric RS.** 2009. Severe acute respiratory syndrome coronavirus papain-like protease ubiquitin-like domain and catalytic domain regulate antagonism of IRF3 and NF-κB signaling. J. Virol. **83:**6689–6705.
17. **Frieman MB, et al.** 2010. SARS-CoV pathogenesis is regulated by a STAT1 dependent but a type I, II and III interferon receptor independent mechanism. PLoS Pathog. **6:**e1000849.
18. **Glass WG, Subbarao K, Murphy B, Murphy PM.** 2004. Mechanisms of host defense following severe acute respiratory syndrome-coronavirus (SARS-CoV) pulmonary infection of mice. J. Immunol. **173:**4030–4039.
19. **Guan Y, et al.** 2003. Isolation and characterization of viruses related to the SARS coronavirus from animals in southern China. Science **302:**276–278.
20. **Harcourt BH, et al.** 2004. Identification of severe acute respiratory syndrome coronavirus replicase products and characterization of papain-like protease activity. J. Virol. **78:**13600–13612.
21. **Holmes KV.** 2005. Structural biology. Adaptation of SARS coronavirus to humans. Science **309:**1822–1823.
22. **Horvat B, et al.** 1996. Transgenic mice expressing human measles virus (MV) receptor CD46 provide cells exhibiting different permissivities to MV infections. J. Virol. **70:**6673–6681.
23. **Hung IF, et al.** 2004. Viral loads in clinical specimens and SARS manifestations. Emerg. Infect. Dis. **10:**1550–1557.
24. **Itoh M, Isegawa Y, Hotta H, Homma M.** 1997. Isolation of an avirulent mutant of Sendai virus with two amino acid mutations from a highly virulent field strain through adaptation to LLC-MK2 cells. J. Gen. Virol. **78(Pt 12):**3207–3215.
25. **Ivanov KA, et al.** 2004. Multiple enzymatic activities associated with severe acute respiratory syndrome coronavirus helicase. J. Virol. **78:** 5619–5632.
26. **Jacomy H, Talbot PJ.** 2001. Susceptibility of murine CNS to OC43 infection. Adv. Exp. Med. Biol. **494:**101–107.
27. **Kalter SS.** 1949. Hemagglutinating behavior of mouse and egg-adapted type A (PR8) influenza virus. Science **110:**184.
28. **Kim GR, McKee KT, Jr.** 1985. Pathogenesis of Hantaan virus infection in suckling mice: clinical, virologic, and serologic observations. Am. J. Trop. Med. Hyg. **34:**388–395.
29. **Ksiazek TG, et al.** 2003. A novel coronavirus associated with severe acute respiratory syndrome. N. Engl. J. Med. **348:**1953–1966.
30. **Kuba K, Imai Y, Penninger JM.** 2006. Angiotensin-converting enzyme 2 in lung diseases. Curr. Opin. Pharmacol. **6:**271–276.
31. **La Monica N, Almond JW, Racaniello VR.** 1987. A mouse model for poliovirus neurovirulence identifies mutations that attenuate the virus for humans. J. Virol. **61:**2917–2920.
32. **Lassnig C, et al.** 2005. Development of a transgenic mouse model susceptible to human coronavirus 229E. Proc. Natl. Acad. Sci. U. S. A. **102:** 8275–8280.
33. **Lau YL, Peiris JS.** 2005. Pathogenesis of severe acute respiratory syndrome. Curr. Opin. Immunol. **17:**404–410.
34. **Lee NR, et al.** 2010. Cooperative translocation enhances the unwinding of duplex DNA by SARS coronavirus helicase nsP13. Nucleic Acids Res. **38:** 7626–7636.

35. **Lee PW, Amyx HL, Gibbs CJ, Jr, Gajdusek DC, Lee HW.** 1981. Propagation of Korean hemorrhagic fever virus in laboratory rats. Infect. Immun. **31**:334–338.

36. **Li F.** 2008. Structural analysis of major species barriers between humans and palm civets for severe acute respiratory syndrome coronavirus infections. J. Virol. **82**:6984–6991.

37. **Li F, Li W, Farzan M, Harrison SC.** 2005. Structure of SARS coronavirus spike receptor-binding domain complexed with receptor. Science **309**:1864–1868.

38. **Li W, et al.** 2005. Receptor and viral determinants of SARS-coronavirus adaptation to human ACE2. EMBO J. **24**:1634–1643.

39. **McCray PB, Jr, et al.** 2007. Lethal infection of K18-hACE2 mice infected with severe acute respiratory syndrome coronavirus. J. Virol. **81**:813–821.

40. **Moore MJ, et al.** 2004. Retroviruses pseudotyped with the severe acute respiratory syndrome coronavirus spike protein efficiently infect cells expressing angiotensin-converting enzyme 2. J. Virol. **78**:10628–10635.

41. **Narayanan K, et al.** 2008. Severe acute respiratory syndrome coronavirus nsp1 suppresses host gene expression, including that of type I interferon, in infected cells. J. Virol. **82**:4471–4479.

42. **Ng MH, et al.** 2010. Immunogenetics in SARS: a case-control study. Hong Kong Med. J. **16**(5 Suppl. 4):29–33.

43. **Ng WF, To KF, Lam WW, Ng TK, Lee KC.** 2006. The comparative pathology of severe acute respiratory syndrome and avian influenza A subtype H5N1—a review. Hum. Pathol. **37**:381–390.

44. **Nicholls JM, et al.** 2006. Time course and cellular localization of SARS-CoV nucleoprotein and RNA in lungs from fatal cases of SARS. PLoS Med. **3**:e27.

45. **Nicholls JM, et al.** 2003. Lung pathology of fatal severe acute respiratory syndrome. Lancet **361**:1773–1778.

46. **Pacciarini F, et al.** 2008. Persistent replication of severe acute respiratory syndrome coronavirus in human tubular kidney cells selects for adaptive mutations in the membrane protein. J. Virol. **82**:5137–5144.

47. **Patrick DM, et al.** 2006. An outbreak of human coronavirus OC43 infection and serological cross-reactivity with SARS coronavirus. Can. J. Infect. Dis. Med. Microbiol. **17**:330–336.

48. **Peiris JS, et al.** 2003. Clinical progression and viral load in a community outbreak of coronavirus-associated SARS pneumonia: a prospective study. Lancet **361**:1767–1772.

49. **Peiris JS, Yuen KY, Osterhaus AD, Stohr K.** 2003. The severe acute respiratory syndrome. N. Engl. J. Med. **349**:2431–2441.

50. **Prentice E, McAuliffe J, Lu X, Subbarao K, Denison MR.** 2004. Identification and characterization of severe acute respiratory syndrome coronavirus replicase proteins. J. Virol. **78**:9977–9986.

51. **Rall GF, et al.** 1997. A transgenic mouse model for measles virus infection of the brain. Proc. Natl. Acad. Sci. U. S. A. **94**:4659–4663.

52. **Ren RB, Costantini F, Gorgacz EJ, Lee JJ, Racaniello VR.** 1990. Transgenic mice expressing a human poliovirus receptor: a new model for poliomyelitis. Cell **63**:353–362.

53. **Roberts A, et al.** 2007. A mouse-adapted SARS-coronavirus causes disease and mortality in BALB/c mice. PLoS Pathog. **3**:e5.

54. **Roberts A, et al.** 2008. Animal models and vaccines for SARS-CoV infection. Virus Res. **133**:20–32.

55. **Roberts A, et al.** 2005. Aged BALB/c mice as a model for increased severity of severe acute respiratory syndrome in elderly humans. J. Virol. **79**:5833–5838.

56. **Rockx B, et al.** 2009. Early upregulation of acute respiratory distress syndrome-associated cytokines promotes lethal disease in an aged-mouse model of severe acute respiratory syndrome coronavirus infection. J. Virol. **83**:7062–7074.

57. **Rockx B, et al.** 2007. Synthetic reconstruction of zoonotic and early human severe acute respiratory syndrome coronavirus isolates that produce fatal disease in aged mice. J. Virol. **81**:7410–7423.

58. **Rota PA, et al.** 2003. Characterization of a novel coronavirus associated with severe acute respiratory syndrome. Science **300**:1394–1399.

59. **Serrano P, et al.** 2009. Nuclear magnetic resonance structure of the nucleic acid-binding domain of severe acute respiratory syndrome coronavirus nonstructural protein 3. J. Virol. **83**:12998–13008.

60. **Sheahan T, et al.** 2008. MyD88 is required for protection from lethal infection with a mouse-adapted SARS-CoV. PLoS Pathog. **4**:e1000240.

61. **Sheahan T, Rockx B, Donaldson E, Corti D, Baric R.** 2008. Pathways of cross-species transmission of synthetically reconstructed zoonotic severe acute respiratory syndrome coronavirus. J. Virol. **82**:8721–8732.

62. **Sheahan T, et al.** 2008. Mechanisms of zoonotic severe acute respiratory syndrome coronavirus host range expansion in human airway epithelium. J. Virol. **82**:2274–2285.

63. **Sheahan T, et al.** 2011. Successful vaccination strategies that protect aged mice from lethal challenge from influenza virus and heterologous severe acute respiratory syndrome coronavirus. J. Virol. **85**:217–230.

64. **Shresta S, Kyle JL, Beatty PR, Harris E.** 2004. Early activation of natural killer and B cells in response to primary dengue virus infection in A/J mice. Virology **319**:262–273.

65. **Shresta S, et al.** 2004. Interferon-dependent immunity is essential for resistance to primary dengue virus infection in mice, whereas T- and B-cell-dependent immunity are less critical. J. Virol. **78**:2701–2710.

66. **Smith MK, et al.** 2006. Human angiotensin-converting enzyme 2 (ACE2) is a receptor for human respiratory coronavirus NL63. Adv. Exp. Med. Biol. **581**:285–288.

67. **Song HD, et al.** 2005. Cross-host evolution of severe acute respiratory syndrome coronavirus in palm civet and human. Proc. Natl. Acad. Sci. U. S. A. **102**:2430–2435.

68. **Sperry SM, et al.** 2005. Single-amino-acid substitutions in open reading frame (ORF) 1b-nsp14 and ORF 2a proteins of the coronavirus mouse hepatitis virus are attenuating in mice. J. Virol. **79**:3391–3400.

69. **Sutton G, et al.** 2004. The nsp9 replicase protein of SARS-coronavirus, structure and functional insights. Structure **12**:341–353.

70. **von Grotthuss M, Wyrwicz LS, Rychlewski L.** 2003. mRNA cap-1 methyltransferase in the SARS genome. Cell **113**:701–702.

71. **Wong SK, Li W, Moore MJ, Choe H, Farzan M.** 2004. A 193-amino acid fragment of the SARS coronavirus S protein efficiently binds angiotensin-converting enzyme 2. J. Biol. Chem. **279**:3197–3201.

72. **Xiao X, Chakraborti S, Dimitrov AS, Gramatikoff K, Dimitrov DS.** 2003. The SARS-CoV S glycoprotein: expression and functional characterization. Biochem. Biophys. Res. Commun. **312**:1159–1164.

73. **Yount B, et al.** 2003. Reverse genetics with a full-length infectious cDNA of severe acute respiratory syndrome coronavirus. Proc. Natl. Acad. Sci. U. S. A. **100**:12995–13000.

74. **Zhao J, Van Rooijen N, Perlman S.** 2009. Evasion by stealth: inefficient immune activation underlies poor T cell response and severe disease in SARS-CoV-infected mice. PLoS Pathog. **5**:e1000636.

75. **Zornetzer GA, et al.** 2010. Transcriptomic analysis reveals a mechanism for a prefibrotic phenotype in STAT1 knockout mice during severe acute respiratory syndrome coronavirus infection. J. Virol. **84**:11297–11309.